PHYSICAL REVIEW ACCELERATORS AND BEAMS **26,** 064402 (2023)

Short-range wakefields in an L-shaped corrugated structure

Weilun Qin,* Martin Dohlus, and Igor Zagorodnov
Deutsches Elektronen-Synchrotron DESY, Notkestr. 85, 22607 Hamburg, Germany

(Received 6 April 2023; accepted 31 May 2023; published 26 June 2023)

We present analytical and numerical studies of short-range wakefields in an L-shaped corrugated structure. This structure has variable streaking polarization and the quadrupole wakefield component is suppressed when the beam moves with equal distances to both plates. These features provide promising capability in multidimensional beam phase space diagnostic and fresh-slice applications. We first give zeroth-order analytical expressions of the longitudinal and the transverse wake functions using the conformal mapping method. Then we combine these results with the first-order approximate formulas of a single-plate structure to obtain more accurate analytical approximations of the wake functions of the L-shaped structure. In order to confirm the accuracy of the analytical model, we have developed a numerical method based on integral equations in the frequency domain for arbitrarily shaped waveguides with surface impedance boundary conditions.

DOI: 10.1103/PhysRevAccelBeams.26.064402

I. INTRODUCTION

X-ray free-electron lasers (XFELs) have been steering scientific applications in a broad range owing to their highest brightness. The customization of the x-ray pulse properties for unique user requirements has involved various types of active or passive devices. Over the past few years, the utilization of the wakefields originated from a metallic corrugated structure [1], also called a dechirper, has successfully demonstrated applications such as electron beam energy chirp control [2,3], multicolor pulse generation [4,5], pulse duration shortening [6,7], and time-resolved diagnostic [8,9] in XFELs. Dielectric structures were also used [10] at XFEL facilities, but so far limited to low electron beam energy.

The passive, metallic corrugated structure was first proposed to be a round one [1] and later built at several FEL facilities to be two parallel plates for better adjustability. In such a flat geometry structure, both the dipole and quadrupole components of the transverse wake exist near the symmetry plane between the two plates. When the electron beam passes through the structure away from the symmetry plane, an extra monopole component of the transverse wake is also excited and streaks the beam transversely. For applications that only utilize the longitudinal wake, such as energy chirp control, two identical parallel-plate sections are usually orthogonally placed with the electron beam passing through the axis to minimize the effect of the quadrupole component [11]. For applications that mainly utilize the monopole kick of the corrugated structure, such as short pulse generation and two-color generation, the electron beam is usually placed far away from the symmetry plane of the two plates or simply only a single plate is used [12–14]. In such a setup, the quadrupole wakefield effect could not be easily compensated and it is favorable to have small β functions at the location of the structure to reduce the time-dependent mismatch along the beam [14,15]. It is worth noting that a small β function at the corrugated structure location also reduces the streaking effect, which can be compensated by a closer distance to the plate.

Recently, an L-shaped corrugated structure with the electron beam passing near the corner of the L-shape was proposed to cancel the quadrupole component of the transverse wakefields while maintaining the streaking strength [16]. Such a structure also allows the possibility to switch between L-shape operation and single-plate operation by adjusting the distances between the electron beam and the two plates. These features of the L-shaped corrugated structure can potentially facilitate "quadrupole-free" streaking of the electron beam in advanced FEL lasing schemes and multidimensional beam phase space diagnostics.

Despite the promising applications, an accurate wakefield model of such a structure has not yet been developed. The calculation of the wakefields for corrugated structures with round and parallel-plate geometry has been performed numerically using the field matching method [11] and time-domain simulations [17–19]. Analytical models for the short bunch wakefields were developed

---

*weilun.qin@desy.de

to the zeroth-order [20] and the first-order [12] approximation, assuming that the impedance of corrugations can be represented by a surface impedance [21]. The first-order model was further extended to single-plate flat geometry by taking the limit of the aperture for the parallel-plate geometry to infinity [13]. In Ref. [16], wakefield calculations for the L-shaped structure were performed numerically in the time domain for a relatively long electron beam.

In this paper, we present an analytical model and a numerical method for calculating the short-range wakefields of the L-shaped corrugated structures. The analytical expressions are given at zeroth-order and at first-order approximations. The zeroth-order formulas are obtained through the conformal mapping method [22,23]. Combining the zeroth-order results with the first-order approximate formulas of a single-plate structure, we obtain more accurate "first-order" analytical approximations for the wake functions of the L-shaped structure. In order to confirm the accuracy of the analytical model, we have developed a numerical method based on integral equations in the frequency domain for arbitrarily shaped waveguides with surface impedance boundary conditions. We assume that the corrugated structure can be described by a surface impedance as it was done for flat geometry in Ref. [21]. The accuracy of such an approach is proven by comparison of the results with those obtained by direct solution of Maxwell's equations in the time domain for a full model of corrugations using ECHO2D [19].

It is of special interest to compare the wakefields of the L-shaped structure to a single-plate one as both operation modes can be realized with the L-shaped structure. The numerical codes, however, have restrictions on the simulated geometries. The integral equation method we developed is capable of calculating steady-state wakefields for arbitrary longitudinally uniform but transversely closed geometry. Open structures such as single-plate and L-shape could be approximated by assuming a rectangle and placing the electron beam toward one plate (for single-plate case) or one corner (for L-shape case). The time-domain code ECHO2D can model only two horizontal corrugated plates placed between two vertical perfectly conducting walls. In this regard, we consider in the paper four different flat geometries shown in Fig. 1. We will show that when the rectangle geometry is properly chosen and the electron beam is properly placed, the effect from the far-away plates can be neglected and it is possible to compare results between different numerical models.

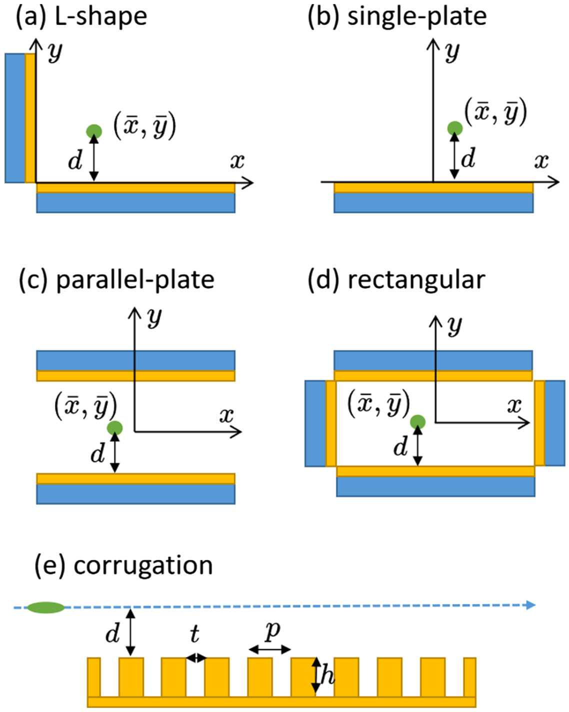

FIG. 1. Sketches of four types of corrugated structure geometries. Front views: (a) L-shape, (b) single-plate, (c) parallel-plate, and (d) rectangular structures. The corrugations are drawn as a yellow layer in the front views and shown with corrugation parameters in the side view (e). The electron beams, located at $(\bar{x}, \bar{y})$, are represented with a green dot in the front view and a green ellipse in the side view. In the side view (e), only the corrugations for the lower plate and its distance to beam d are shown for simplicity.

The four geometries studied here are sketched in Fig. 1, namely, (a) L-shape, (b) single-plate, (c) parallel-plate, and (d) rectangular structures. The geometries are shown as front views and the corrugations are drawn as a yellow layer therein. The side view of the corrugations and corresponding corrugation parameters are shown in Fig. 1(e). For the unbounded geometries in Figs. 1(a)–1(c), the plates are assumed to be wide enough so that they can be treated as they extend to infinity. The electron beams, located at $(\bar{x}, \bar{y})$, are represented with a green dot in the front view and a green ellipse in the side view. It should be noted that in this paper, the electron beam is not fixed at the shown location but can move freely toward or away from any corrugated plate.

The rest of this paper is organized as follows: We first give zeroth-order analytical formulas for the wakefields of the studied geometries in Sec. II A. Then, in Sec. II B, we summarize the existing first-order analytical approximation for single-plate and parallel-plate structures and propose first-order analytical expressions for the L-shaped structure. Numerical methods are introduced in Sec. III. In Sec. IV, we first show that with a proper choice of the rectangle geometry, the single-plate and the L-shape structures can be simulated. Then, we give examples of a single-plate structure and an L-shaped structure to show the validity of the analytical formulas and numerical methods. The features of the L-shaped corrugated structure are discussed. Finally, we give concluding remarks in Sec. V.

II. ANALYTICAL METHODS

In the following, we will work in a Cartesian coordinate system, where x is the horizontal coordinate and

y is the vertical one. The longitudinal wake function $w_{\parallel}(x, y, x_0, y_0, s)$ describes the energy loss of the witness particle with transverse coordinates (x, y) caused by the source particle with transverse coordinates (x_0, y_0), which moves ahead of the witness particle by a longitudinal distance s. The transverse wake function can be found through the Panofsky-Wenzel theorem:

$$\frac{\partial}{\partial s}\vec{w}_{\perp} = -\nabla_{\perp} w_{\parallel}. \tag{1}$$

For geometries considered in this paper, the components of the transverse wake function near a reference trajectory with coordinates $(\bar{x}, \bar{y})$ can be presented through expansion:

$$w_x(x, y, x_0, y_0, s) \approx w_{xm}(\bar{x}, \bar{y}, s) + w_d(\bar{x}, \bar{y}, s)(x_0 - \bar{x}) - w_q(\bar{x}, \bar{y}, s)(x - \bar{x}), \tag{2}$$

$$w_y(x, y, x_0, y_0, s) \approx w_{ym}(\bar{x}, \bar{y}, s) + w_d(\bar{x}, \bar{y}, s)(y_0 - \bar{y}) + w_q(\bar{x}, \bar{y}, s)(y - \bar{y}). \tag{3}$$

The coefficients of the expansion w_{xm}, w_{ym} are the monopole transverse wake functions in x and y directions. The other coefficients w_d, w_q are dipole and quadrupole transverse wake functions, respectively. We note that in Refs. [12,13], the "dipole" component was what is referred to as the monopole component here. Other linear terms in the expansion are neglected. In the following, we are looking for the analytical approximation of these coefficients.

A. Zeroth-order approximation

It has been shown [22–24] that exact calculations of the upper limits of the longitudinal electric field and of the transverse component of the Lorentz force can be obtained by the conformal mapping technique. This method applies to longitudinally homogeneous waveguides with arbitrary retarding layers (which in our case are the corrugations). In this analysis, the cross section of the waveguide is represented in a complex plane $z = x + iy$ and conformally mapped onto a disk with radius a in another complex plane ω. The location of the source particle z_0 is mapped to the center of the disk $\omega_0 = 0$. Knowing the conformal mapping as $\omega = f(z, z_0)$, the upper limits of the longitudinal electric field and of the transverse component of the Lorentz force can be obtained through its derivatives with respect to z by [24]

$$E_{\parallel}(z, z_0, 0^+) = -\frac{Z_0 c}{\pi}\frac{Q}{a^2}\Re[f'(z, z_0)^* f'(z_0, z_0)], \tag{4}$$

$$\frac{\partial}{\partial s}F_{\perp}(z, z_0, 0^+) = \frac{Z_0 c}{\pi}\frac{qQ}{a^2} f''(z, z_0)^* f'(z_0, z_0), \tag{5}$$

where $\Re$ denotes the real part, $Z_0 = 377\ \Omega$ is the vacuum impedance, c is the speed of light in vacuum, s is the longitudinal distance behind the source particle, Q is the charge of the source particle, q is the charge of the witness particle, and the asterisks denote the complex conjugation. Here $F_{\perp}$ is a complex function defined as $F_{\perp} = F_x + iF_y$ with F_x and F_y being the x and y components of the force.

For simplicity, we define the longitudinal and transverse form factors as

$$\mathbb{F}_{\parallel}(z, z_0) = \Re[f'(z, z_0)^* f'(z_0, z_0)], \tag{6}$$

$$\mathbb{F}_{\perp}(z, z_0) = f''(z, z_0)^* f'(z_0, z_0). \tag{7}$$

The longitudinal and transverse wakes can be then approximated via

$$w_{\parallel}(z, z_0, s) \approx -\frac{E_{\parallel}(z, z_0, 0^+)}{Q}\theta(s) = \frac{Z_0 c}{\pi a^2}\mathbb{F}_{\parallel}(z, z_0)\theta(s), \tag{8}$$

$$w_{\perp}(z, z_0, s) \approx \frac{s}{qQ}\frac{\partial}{\partial s}F_{\perp}(z, z_0, 0^+)\theta(s) = \frac{Z_0 c s}{\pi a^2}\mathbb{F}_{\perp}(z, z_0)\theta(s), \tag{9}$$

where $\theta(s)$ is the Heaviside step function. Similarly, the transverse wake $w_{\perp}$ is expressed as a complex function with $w_{\perp} = w_x + iw_y$.

1. Single-plate structure

For the single-plate case, the corrugated plate is put at $y = 0$ and faces the upper half plane. The conformal mapping from the upper half plane in the z plane to a disk with a radius of a is given by [25]

$$\psi(z) = a\frac{z - i}{z + i}. \tag{10}$$

Assuming the source particle is located at z_0 in the upper half plane, the corresponding location in ψ plane can be found with $\psi_0 = \psi(z_0)$. The disk can be further mapped to another disk in ω plane with the same radius a and ψ_0 mapped to the center of the disk using

$$\omega(\psi) = a^2\frac{\psi - \psi_0}{a^2 - \psi\psi_0^*}, \tag{11}$$

where ψ_0^* is the complex conjugate of ψ_0. Combine the above mapping, it is then found that the conformal mapping from the upper half plane to a disk with source particle at z_0 mapped to the center of the disk can be expressed as

$$f(z, z_0) = -a\frac{z_0^* - i}{z_0 + i}\frac{z - z_0}{z - z_0^*}. \tag{12}$$

With Eq. (12), we obtain the form factors for the single-plate structure as

$$\mathbb{F}_{\parallel}(z,z_0) = -a^2\mathfrak{R}\left[\frac{1}{(z_0-z^*)^2}\right], \tag{13}$$

$$\mathbb{F}_{\perp}(z,z_0) = 2ia^2\frac{z_0-\mathfrak{R}(z_0)}{(z_0-z^*)^3\mathfrak{I}(z_0)}, \tag{14}$$

where $\mathfrak{I}$ denotes the imaginary part. Taking $z = x + iy$ and $z_0 = x_0 + iy_0$, we obtain the longitudinal and transverse wakes as a function of the transverse position of the source and witness particles:

$$w_{\parallel}^{S}(x,y,x_0,y_0,s) = -\frac{Z_0c}{\pi}\mathfrak{R}\left[\frac{1}{(x_0-x+i(y_0+y))^2}\right]\theta(s), \tag{15}$$

$$w_{\perp}^{S}(x,y,x_0,y_0,s) = -\frac{2Z_0c}{\pi}\frac{s}{(x_0-x+i(y_0+y))^3}\theta(s), \tag{16}$$

here S stands for single-plate structure.

The longitudinal wake is usually taken when $x = x_0 = \bar{x}$ and $y = y_0 = \bar{y}$, giving

$$w_{\parallel}^{S}(\bar{y},s) = A_{\parallel}^{S}(\bar{y})\theta(s), \qquad A_{\parallel}^{S}(\bar{y}) = \frac{Z_0c}{4\pi}\frac{1}{\bar{y}^2}. \tag{17}$$

We note that in the above expressions, the distance from the beam reference position to the plate is $\bar{y}$. This result is the same as obtained in Ref. [13].

For the transverse wake, we first obtain w_x and w_y as

$$w_x^S = \frac{2Z_0c}{\pi}\frac{(x-x_0)[(x-x_0)^2-3(y+y_0)^2]}{[(x-x_0)^2+(y+y_0)^2]^3}s\theta(s), \tag{18}$$

$$w_y^S = -\frac{2Z_0c}{\pi}\frac{(y+y_0)[-3(x-x_0)^2+(y+y_0)^2]}{[(x-x_0)^2+(y+y_0)^2]^3}s\theta(s). \tag{19}$$

Following Eqs. (2) and (3), we obtain the transverse monopole, dipole, and quadrupole components for the single-plate structures as

$$w_{xm}^{S}(\bar{y},s) = 0, \tag{20}$$

$$w_{ym}^{S}(\bar{y},s) = A_{m}^{S}(\bar{y})s\theta(s), \qquad A_{m}^{S}(\bar{y}) = -\frac{Z_0c}{4\pi}\frac{1}{\bar{y}^3}, \tag{21}$$

$$w_{d}^{S}(\bar{y},s) = A_{d}^{S}(\bar{y})s\theta(s), \qquad A_{d}^{S}(\bar{y}) = \frac{Z_0c}{\pi}\frac{3}{8\bar{y}^4}, \tag{22}$$

$$w_{q}^{S}(\bar{y},s) = w_{d}^{S}(\bar{y},s). \tag{23}$$

The results we obtained here are in agreement with the results from Ref. [13].

2. Parallel-plate structure

The parallel-plate geometry is modeled as parallel strips with plates located at $y = \pm a$. The conformal mapping from the parallel strips to a disk with the source location z_0 mapped to the center of the disk is found to be [24]

$$f(z,z_0) = \frac{ia[\tanh(\frac{\pi z}{4a}) - \tanh(\frac{\pi z_0}{4a})]}{1-\tanh(\frac{\pi z}{4a})\tanh(\frac{\pi z_0^*}{4a})}. \tag{24}$$

Inserting the mapping into Eqs. (6) and (7), we obtain the form factors for parallel-plate geometry as

$$\mathbb{F}_{\parallel}(z,z_0) = \frac{\pi^2}{16}\mathfrak{R}\left\{\operatorname{sech}^2\left[\frac{\pi(z_0-z^*)}{4a}\right]\right\}, \tag{25}$$

$$\mathbb{F}_{\perp}(z,z_0) = \frac{\pi^3}{32a}\operatorname{sech}^2\left[\frac{\pi(z_0-z^*)}{4a}\right]\tanh\left[\frac{\pi(z_0-z^*)}{4a}\right]. \tag{26}$$

Substituting with $z = x + iy$ and $z_0 = x_0 + iy_0$, we obtain the longitudinal and transverse wakes as a function of the transverse position of the source and witness particles:

$$w_{\parallel}^{P}(x,y,x_0,y_0,s) = \frac{\pi Z_0c}{16a^2}\mathfrak{R}\left\{\operatorname{sech}^2\left[\frac{\pi[x-x_0-i(y+y_0)]}{4a}\right]\right\}\theta(s), \tag{27}$$

$$w_{\perp}^{P}(x,y,x_0,y_0,s) = \frac{\pi^2Z_0cs}{32a^3}\operatorname{sech}^2\left[\frac{\pi[x_0-x+i(y+y_0)]}{4a}\right] \times\tanh\left[\frac{\pi[x_0-x+i(y+y_0)]}{4a}\right]\theta(s), \tag{28}$$

where P stands for parallel plates.

By taking $x = x_0 = \bar{x}$ and $y = y_0 = \bar{y}$, we obtain the longitudinal wake for parallel-plate structure as

$$w_{\parallel}^{P}(\bar{y},s) = A_{\parallel}^{P}(\bar{y})\theta(s), \quad A_{\parallel}^{P}(\bar{y}) = \frac{\pi Z_0c}{16a^2}\sec^2\left(\frac{\pi\bar{y}}{2a}\right). \tag{29}$$

Note that here the distance from the beam reference position to the upper plate is $a - \bar{y}$.

For the transverse wake, we again use $w_{\perp} = w_x + iw_y$ to obtain w_x and w_y, then expand in Taylor series near the reference trajectory $\bar{x}$ and $\bar{y}$ to get monopole, dipole, and quadrupole transverse wake functions. The coefficients of the expansion are as follows:

$$w_{xm}^{P}(\bar{y},s) = 0, \tag{30}$$

$$w_{ym}^P(\bar{y},s) = A_m^P(\bar{y}) s\theta(s),$$
$$A_m^P(\bar{y}) = \frac{Z_0 c}{4\pi}\frac{\pi^3}{8a^3}\sec^2\left(\frac{\pi\bar{y}}{2a}\right)\tan\left(\frac{\pi\bar{y}}{2a}\right), \tag{31}$$

$$w_d^P(\bar{y},s) = A_d^P(\bar{y}) s\theta(s),$$
$$A_d^P(\bar{y}) = \frac{Z_0 c}{4\pi}\frac{\pi^4}{32a^4}\left[2-\cos\left(\frac{\pi\bar{y}}{a}\right)\right]\sec^4\left(\frac{\pi\bar{y}}{2a}\right), \tag{32}$$

$$w_q^P(\bar{y},s) = w_d^P(\bar{y},s). \tag{33}$$

The results we obtained here are in agreement with the results from Ref. [12].

3. L-shaped structure

The L-shaped geometry is modeled as the first quadrant of a Cartesian coordinate system, with the two plates located at $y=0$ and $x=0$, respectively. The corrugations of the two plates face toward the first quadrant. The conformal mapping from the first quadrant in the z plane to a disk in ω plane with the source location z_0 mapped to the center of the disk is found to be [25]

$$f(z,z_0) = -a\frac{z_0^{*2}-i}{z_0^2+i}\frac{z^2-z_0^2}{z^2-z_0^{*2}}. \tag{34}$$

The form factors for the L-shaped structure then follow as

$$\mathbb{F}_\parallel(z,z_0) = -4a^2\Re\left[\frac{z_0 z^*}{(z_0^2-z^{*2})^2}\right], \tag{35}$$

$$\mathbb{F}_\perp(z,z_0) = -\frac{4a^2 z_0(z_0^2+3z^{*2})}{(z_0^2-z^{*2})^3}. \tag{36}$$

Substituting with $z=x+iy$ and $z_0=x_0+iy_0$, we obtain the longitudinal and transverse wakes as a function of the transverse position of the source and witness particles:

$$\begin{aligned} w_\parallel^L(x,y,x_0,y_0,s) &= -\frac{4Z_0 c}{\pi}\Re\left\{\frac{(x-iy)(x_0+iy_0)}{[(x-iy)^2-(x_0+iy_0)^2]^2}\right\} \\ &= w_\parallel^S(x,y,x_0,y_0,s) + w_\parallel^S(y,x,y_0,x_0,s), \end{aligned} \tag{37}$$

$$\begin{aligned} w_\perp^L(x,y,x_0,y_0,s) &= w_\perp^S(x,y,x_0,y_0,s) \\ &\quad + i w_\perp^S(y,x,y_0,x_0,s)^*, \end{aligned} \tag{38}$$

where L stands for L-shaped structure. Eqs. (37) and (38) mean that in zeroth-order approximation, the wake functions of the L-shaped structure can be obtained as a direct sum of the wake functions of the single plates.

Taking the longitudinal wake at the reference trajectory $x=x_0=\bar{x}$, $y=y_0=\bar{y}$, we have

$$w_\parallel^L(\bar{x},\bar{y},s) = (A_\parallel^S(\bar{x}) + A_\parallel^S(\bar{y}))\theta(s). \tag{39}$$

Comparing the result with Eq. (17), we see that at zeroth order, when the beam has an equal distance toward the two plates, $\bar{y}=\bar{x}$, the L-shaped corrugated structure generates twice the longitudinal wake as the single-plate structure.

Similarly, for the transverse wake, we again use $w_\perp = w_x + i w_y$ to obtain w_x and w_y, then expand in the Taylor series to get monopole, dipole, and quadrupole wakes for x and y, respectively. We have

$$w_{xm}^L(\bar{x},\bar{y},s) = A_m^S(\bar{x}) s\theta(s), \tag{40}$$

$$w_{ym}^L(\bar{x},\bar{y},s) = A_m^S(\bar{y}) s\theta(s), \tag{41}$$

$$w_d^L(\bar{x},\bar{y},s) = [A_d^S(\bar{x}) + A_d^S(\bar{y})] s\theta(s), \tag{42}$$

$$w_q^L(\bar{x},\bar{y},s) = [A_d^S(\bar{y}) - A_d^S(\bar{x})] s\theta(s). \tag{43}$$

Compared to the single-plate structure, when $\bar{y}=\bar{x}$, the total monopole kick strength is increased by a factor of $\sqrt{2}$ and rotated by $\pi/4$. The dipole wake is twice as large. The quadrupole wake is canceled. Taking $\bar{x}\to\infty$, the results of the single plate are recovered. The results at zeroth order already indicate a few unique features of the L-shaped corrugated structure. First, it is possible to operate the structure in either L-shape mode or single-plate mode by properly adjusting the distance between the electron beam and the plates. Second, in the L-shape operation mode, the overall streaking is enhanced compared with a single plate, and it is possible to realize "quadruple-free" streaking.

4. Rectangular structure

The conformal mapping from a rectangle with half-width b and half-height a in z plane to a disk with radius a in ψ plane takes the form [26]

$$\psi(z) = a\frac{1+i\sqrt{\kappa}\,\mathrm{sn}(\frac{ia+z}{b}K,\kappa^2)}{i+\sqrt{\kappa}\,\mathrm{sn}(\frac{ia+z}{b}K,\kappa^2)}. \tag{44}$$

Here sn is the Jacobi elliptic sine function with

$$\kappa = \left(\frac{\theta_2(0,m)}{\theta_3(0,m)}\right)^2, \quad K = \frac{\pi}{2}\theta_3^2(0,m), \quad m = e^{-2\pi a/b}, \tag{45}$$

where θ_2 and θ_3 are the Jacobi theta functions. Here, the source location z_0 is mapped to $\psi_0 = \psi(z_0)$. Using Eq. (11), we further center the source location and obtain

$$f(z,z_0) = a\frac{[1+i\sqrt{\kappa}\,\mathrm{sn}(\xi_0)^*][\mathrm{sn}(\xi)-\mathrm{sn}(\xi_0)]}{[\sqrt{\kappa}\,\mathrm{sn}(\xi_0)+i][\mathrm{sn}(\xi_0)^*-\mathrm{sn}(\xi)]}. \tag{46}$$

Here we have used $\xi = \frac{ia+z}{b}K$, $\xi_0 = \frac{ia+z_0}{b}K$, and omitted κ^2 in the second argument of the sn function for simplicity.

Using the mapping in Eq. (46), we obtain the expressions of longitudinal and transverse wakes for a rectangular structure as functions of the positions of the source and witness particles

$$w_{\parallel}^{R}(z,z_0,s) = -\frac{Z_0 c K^2}{\pi b^2}\mathfrak{R}\left\{\frac{\mathrm{cn}(\xi_0)\mathrm{dn}(\xi_0)\mathrm{cn}(\xi)^*\mathrm{dn}(\xi)^*}{[\mathrm{sn}(\xi)^* - \mathrm{sn}(\xi_0)]^2}\right\}\theta(s), \tag{47}$$

$$w_{\perp}^{R}(z,z_0,s) = -\frac{Z_0 c K^3 s}{\pi b^3}\frac{\mathrm{cn}(\xi_0)\mathrm{dn}(\xi_0)\{\mathrm{dn}^2(\xi)[\mathrm{sn}(\xi_0)^* - \mathrm{sn}(\xi)]\mathrm{sn}(\xi) - \mathrm{cn}^2(\xi)[-\mathrm{sn}(\xi_0)^*\mathrm{sn}(\xi)\kappa^2 + \mathrm{dn}^2(\xi) + 1]\}^*}{[\mathrm{sn}(\xi)^* - \mathrm{sn}(\xi_0)]^3}\theta(s). \tag{48}$$

Here, cn, dn, and sn are Jacobi elliptic functions.

For the longitudinal wake, at the source particle location, $z = z_0 = \bar{z} = \bar{x} + i\bar{y}$, we have

$$w_{\parallel}^{R}(\bar{z},s) = \frac{Z_0 c K^2}{4\pi b^2}\frac{|\mathrm{cn}(\bar{\xi})|^2|\mathrm{dn}(\bar{\xi})|^2}{\mathfrak{I}[\mathrm{sn}(\bar{\xi})]^2}\theta(s), \tag{49}$$

where $\bar{\xi} = \frac{ia+\bar{z}}{b}K$ and $|\mathrm{cn}|$ means to take the modulus. For the case that the source particle is located at the center of the rectangle, $\bar{z} = 0$, we have

$$w_{\parallel}^{R}(0,s) = \frac{Z_0 c K^2}{4\pi b^2}\frac{|\mathrm{cn}(iKa/b)|^2|\mathrm{dn}(iKa/b)|^2}{\mathfrak{I}[\mathrm{sn}(iKa/b)]^2}\theta(s). \tag{50}$$

Further assuming $a/b \to 0$, we recover the results for parallel-plate geometry: $w_{\parallel}^{R}(0,s) = w_{\parallel}^{P}(0,s)$.

For the transverse wake, here we only give the monopole wake for a rectangular structure by taking $z = z_0 = \bar{z}$, as

$$w_{m}^{R}(\bar{z},s) = -\frac{Z_0 c K^3 s}{\pi b^3}\frac{\mathrm{cn}(\bar{\xi})\mathrm{dn}(\bar{\xi})\{\mathrm{dn}^2(\bar{\xi})[|\mathrm{sn}(\bar{\xi})|^2 - \mathrm{sn}(\bar{\xi})^2] - \mathrm{cn}^2(\bar{\xi})[-|\mathrm{sn}(\bar{\xi})|^2\kappa^2 + \mathrm{dn}^2(\bar{\xi}) + 1]\}^*}{[\mathrm{sn}(\bar{\xi})^* - \mathrm{sn}(\bar{\xi})]^3}\theta(s). \tag{51}$$

B. First-order approximation

The above analysis by means of conformal mapping gives a zeroth-order approximation of the wake functions, where the longitudinal wake is a constant and the transverse wakes have constant slopes. The zeroth-order approximation gives the upper limits of the wake functions and is valid for extremely short bunches. For longer bunches, the deviation from the zeroth-order approximation can be large. Therefore, it is necessary to develop a higher-order approximation of the wake functions. For the corrugated structures, such an approximation has been developed using a surface impedance approach.

The use of the surface impedance concept for calculating the beam impedance in accelerators was first introduced to study the impedance of surface roughness [27]. It is defined as the ratio of the longitudinal electric field and the azimuthal magnetic field on the surface. Several surface impedance models have been developed for roughness [27,28] and small, periodic corrugations [29–31].

It was shown in Ref. [12] that the interaction of the charged beam with the perfectly conducting flat corrugated structure can be described by the same surface impedance as for an infinite chain of pillboxes [32]:

$$Z_S(k) = Z_0\frac{1+i}{\sqrt{ks_c}}, \qquad s_c = \frac{\pi}{t}(\alpha(t/p)p)^2, \tag{52}$$

with $\alpha(x) = 1 - 0.465\sqrt{x} - 0.070x$, and t, p being the corrugation parameters. Using this surface impedance, Bane and Stupakov derived the generalized longitudinal and transverse impedance for calculating wakefields in parallel-plate geometry with boundaries at $y = \pm a$ in Ref. [21]. First-order approximation has then been derived for parallel-plate structure [12] and single-plate structure [13], respectively. In the following, we first give an overview of the obtained wakes for parallel-plate and single-plate structures, then we combine the formal expression with the zeroth-order approximation obtained in the previous section to give a first-order approximation for the L-shaped structure.

1. Parallel-plate structure

The longitudinal wake function for the source and witness charges at position $\bar{y}$ can be approximated by an exponential function

$$w_{\parallel}^{P1}(\bar{y},s) = A_{\parallel}^{P}(\bar{y})e^{-\sqrt{\frac{s}{s_{\parallel}(\bar{y})}}}\theta(s), \tag{53}$$

where $P1$ stands for first-order approximation of parallel-plate structure, $A_{\parallel}^{P}(\bar{y})$ is given in Eq. (29) and

$$s_{\parallel}(\bar{y}) = 4s_r\left(1 + \frac{1}{3}\cos^2\beta + \beta\tan\beta\right)^{-2},$$

$$\beta = \frac{\pi\bar{y}}{2a}, \qquad s_r = \frac{a^2}{2s_c}. \tag{54}$$

The transverse monopole wake function can be approximated as

$$w_{ym}^{P1}(\bar{y},s) = 2A_m^P(\bar{y})s_m(\bar{y}) \times \left[1-\left(1+\sqrt{\frac{s}{s_m(\bar{y})}}\right)e^{-\sqrt{\frac{s}{s_m(\bar{y})}}}\right]\theta(s), \quad (55)$$

where $A_m^P(\bar{y})$ is given in Eq. (31) and the characteristic distance reads

$$s_m(\bar{y}) = 4s_r\left(\frac{3}{2}-\beta\cot 2\beta+2\beta\csc 2\beta\right)^{-2}. \quad (56)$$

The same form of the expression Eq. (55) can be used to approximate the dipole and quadrupole wake functions. The coefficient $A_d^P(\bar{y})$ is given in Eq. (32) and the quadrupole coefficient coincides with the dipole one: $A_q^P(\bar{y}) = A_d^P(\bar{y})$. From Ref. [12], the characteristic distance for the quadrupole wake is

$$s_q(\bar{y}) = 4s_r\left(\frac{56-\cos 2\beta}{30}+\frac{0.3+\beta\sin 2\beta}{2-\cos 2\beta}+2\beta\tan\beta\right)^{-2}. \quad (57)$$

Following the same procedure, we can derive the dipole coefficient not considered earlier in Ref. [12]

$$s_d(\bar{y}) = 4s_r\left(\frac{64+\cos 2\beta}{30}-\frac{0.3-\beta\sin 2\beta}{2-\cos 2\beta}+2\beta\tan\beta\right)^{-2}. \quad (58)$$

2. Single-plate structure

For the single-plate structure, the first-order wake functions are approximated by the same formal expressions as in the previous section. The coefficients $A_\parallel^S(\bar{y})$, $A_m^S(\bar{y})$, $A_d^S(\bar{y})$ are obtained above in Eqs. (17), (21), (22), and $A_q^S(\bar{y}) = A_d^S(\bar{y})$. If we define $\bar{y}$ as the distance to the plate, then in the limit $a \to \infty$, Eqs. (54) and (56)–(58) reduce to the expressions

$$s_\parallel(\bar{y}) = \frac{2\bar{y}^2}{s_c}, \quad (59)$$

$$s_m(\bar{y}) = \frac{8\bar{y}^2}{9s_c}, \quad (60)$$

$$s_d(\bar{y}) = s_q(\bar{y}) = \frac{\bar{y}^2}{2s_c}, \quad (61)$$

and the wake functions can be written as

$$w_\parallel^{S1}(\bar{y},s) = A_\parallel^S(\bar{y})e^{-\sqrt{\frac{s}{s_\parallel(\bar{y})}}}\theta(s), \quad (62)$$

$$w_{xm}^{S1}(\bar{y},s) = 0, \quad (63)$$

$$w_{ym}^{S1}(\bar{y},s) = 2A_m^S(\bar{y})s_m(\bar{y}) \times \left[1-\left(1+\sqrt{\frac{s}{s_m(\bar{y})}}\right)e^{-\sqrt{\frac{s}{s_m(\bar{y})}}}\right]\theta(s), \quad (64)$$

$$w_d^{S1}(\bar{y},s) = 2A_d^S(\bar{y})s_d(\bar{y})\left[1-\left(1+\sqrt{\frac{s}{s_d(\bar{y})}}\right)e^{-\sqrt{\frac{s}{s_d(\bar{y})}}}\right]\theta(s), \quad (65)$$

$$w_q^{S1}(\bar{y},s) = w_d^{S1}(\bar{y},s). \quad (66)$$

Let us note that we corrected the expression for s_q published earlier in Ref. [13].

3. L-shaped structure

We assume that Eqs. (37) and (38) hold for the first-order approximation as well and the wake functions of the L-shaped structure can be obtained as a direct sum of the wake functions of the single plates.

If we define $\bar{x}, \bar{y}$ as the distance to the plates, then we obtain

$$w_\parallel^{L1}(\bar{x},\bar{y},s) = w_\parallel^{S1}(\bar{x},s) + w_\parallel^{S1}(\bar{y},s), \quad (67)$$

where $w_\parallel^{S1}$ is given by Eq. (62). The transverse wake functions are

$$w_{xm}^{L1}(\bar{x},\bar{y},s) = w_{ym}^{S1}(\bar{x},s), \quad (68)$$

$$w_{ym}^{L1}(\bar{x},\bar{y},s) = w_{ym}^{S1}(\bar{y},s), \quad (69)$$

$$w_d^{L1}(\bar{x},\bar{y},s) = w_d^{S1}(\bar{y},s) + w_d^{S1}(\bar{x},s), \quad (70)$$

$$w_q^{L1}(\bar{x},\bar{y},s) = w_d^{S1}(\bar{y},s) - w_d^{S1}(\bar{x},s), \quad (71)$$

where w_{ym}^{S1}, w_d^{S1} are given by Eqs. (64) and (65). When $\bar{x} \to \infty$, the equations agree with those of a single-plate.

III. NUMERICAL METHODS

A. Integral equation method in frequency domain

In the following, we present a numerical scheme to calculate the high-frequency impedance of relativistic point charge. It is based on the boundary element method. This numerical technique allows us to calculate the steady-state wake function for an arbitrary cross section of the pipe. Our equations and the approach are similar to those presented in Ref. [26] for resistive wall conductivity. However, we use different integral equations and different numerical methods. Let us describe shortly our numerical method and the obtained results.

The charge of a relativistic bunch in the frequency domain reads $\rho(x,y)e^{i(\omega t-kz)}$, $\omega = kc$, where z is the longitudinal coordinate, k is the wave number. Due to the linearity of the Maxwell equations, all other quantities of interest will have the same form. Hence the Maxwell equations in the frequency domain can be reduced to the second-order differential equations for the transverse components of the electromagnetic field, $\vec{E}_\perp = (E_x, E_y)^T$, $\vec{H}_\perp = (H_x, H_y)^T$, in the pipe cross section S:

$$\Delta_\perp \vec{E}_\perp = \epsilon_0^{-1}\vec{\nabla}_\perp \rho, \qquad \Delta_\perp \vec{H}_\perp = \vec{0}, \tag{72}$$

where ϵ_0 is the permittivity of the vacuum and the transverse operators are defined by expressions $\Delta_\perp = \partial_x^2 + \partial_y^2$, $\vec{\nabla}_\perp = (\partial_x, \partial_y)^T$. Here symbols ∂_x, ∂_y mean the partial derivatives in the transverse directions.

The longitudinal components of the electromagnetic field can be found through the transverse ones

$$E_z = \frac{1}{ik}\left(\nabla_\perp \vec{E}_\perp - \frac{\rho}{\epsilon_0}\right), \qquad H_z = \frac{1}{ik}\nabla_\perp \vec{H}_\perp. \tag{73}$$

It is shown in Appendix A that the surface impedance boundary condition in the high-frequency approximation, $k \gg 1$, can be written as

$$E_z = \frac{Z_s}{Z_0}E_n, \qquad E_t = 0. \tag{74}$$

Let us present the full electric field $\vec{E}_\perp$ at the position $\vec{r} = (x, y)^T$ of the point charge e at the position $\vec{r}_0 = (x_0, y_0)^T$ as the sum

$$\vec{E}_\perp = \vec{E}_\perp^s + \vec{E}_\perp^0, \tag{75}$$

where $\vec{E}_\perp^0 = e(\vec{r} - \vec{r}_0)(2\pi\epsilon_0 c|\vec{r} - \vec{r}_0|^2)^{-1}$ is the field of the point charge in the free space and $\vec{E}_\perp^s$ is the field scattered from the surface of the pipe. The components of the scattered field fulfill the boundary value problem for the Laplace equation

$$\Delta_\perp \vec{E}_\perp^s = 0, \qquad \vec{r} \in S, \tag{76}$$

with the boundary conditions

$$\frac{1}{ik}\nabla_\perp \vec{E}_\perp^s + \frac{Z_s}{Z_0}\vec{n}\vec{E}_\perp^s = -\frac{Z_s}{Z_0}\vec{n}\vec{E}_\perp^0, \tag{77}$$

$$\vec{\tau}\vec{E}_\perp^s = -\vec{\tau}\vec{E}_\perp^0, \qquad \vec{r} \in \partial S, \tag{78}$$

where $\vec{\tau} = (-n_y, n_x)^T$ is the tangential vector to the pipe contour ∂S and we have used the relations $E_z^s = (ik)^{-1}\nabla_\perp \vec{E}_\perp^s$, $E_z^0 = 0$ in the boundary conditions given by Eq. (74).

Let us introduce an integral operator A of a simple layer

$$[Af](\vec{r}) = 2\pi \int_{\partial S} G(\vec{r} - \vec{r'})f(\vec{r'})ds(\vec{r'}), \qquad \vec{r} \in S, \tag{79}$$

where $G(\vec{r}) = (2\pi)^{-1}\log(|\vec{r}|)$ is the Green function of the two-dimensional Laplace operator.

We present the transverse components of the electric field E_x^s and E_y^s in form of the simple layer, Eq. (79), with unknown charge densities q_x and q_y, correspondingly. Then the boundary conditions, Eqs. (77) and (78), can be rewritten as a boundary integral equation with unknown charge densities q_x and q_y on the pipe boundary ∂S

$$\begin{pmatrix} \pi n_x + \partial_x A + \alpha n_x A & \pi n_y + \partial_y A + \alpha n_y A \\ -n_y A & n_x A \end{pmatrix}\begin{pmatrix} q_x \\ q_y \end{pmatrix} = \begin{pmatrix} -\alpha(n_x E_x^0 + n_y E_y^0) \\ n_y E_x^0 - n_x E_y^0 \end{pmatrix}, \tag{80}$$

where $\alpha = ik\frac{Z_s}{Z_0}$, and the integral operator $\partial_x A$ is defined as

$$[\partial_x A f](\vec{r}) = \int_{\partial S} \frac{x - x'}{|\vec{r} - \vec{r'}|^2} f(\vec{r'})ds(\vec{r'}), \qquad \vec{r} \in \partial S. \tag{81}$$

The integral operator $\partial_y A$ has a similar form. For $\vec{r}$ on the pipe boundary ∂S, the integral has to be calculated as Cauchy principal value. Here we have used the relation [33]

$$\nabla_\perp [Af](\vec{r}) = [\nabla_\perp A f](\vec{r}) + \pi \vec{n} f(\vec{r}), \qquad \vec{r} \in \partial S. \tag{82}$$

The approximation of the singular integrals and the numerical method of the solution are outlined in Appendix B.

If the charge densities q_x and q_y are known then the longitudinal impedance can be found from the longitudinal electric field

$$Z_{\|}(\vec{r}, \vec{r_0}, \omega) = \frac{-E_z(\vec{r})}{ec},$$
$$E_z(\vec{r}) = \frac{1}{ik}([\partial_x A q_x](\vec{r}) + [\partial_y A q_y](\vec{r})), \qquad \vec{r} \in S. \tag{83}$$

The point charge longitudinal wake function can then be found through an inverse Fourier transform of the impedance.

B. Finite-difference method in time domain

Another numerical method we use in this paper is the finite-difference method in time domain. Here we obtain the wake for a short Gaussian bunch using the time domain, wakefield solving program for “rectangular” geometry ECHO2D [19]. The code can solve the problems for the parallel-plate geometry shown in Fig. 1(c). It models accurately the corrugated geometry between two conductive walls with distance w. The single-plate geometry can also be approximated if the beam is close to one plate while far enough away from the other plate. The code is not able to simulate L-shaped or rectangular geometries with corrugations on all four walls.

In ECHO2D, the longitudinal wake potential is found through modal expansion in the form

$$W_{\|}(x,y,x_0,y_0,s) = \frac{1}{w}\sum_{m=1}^{\infty} W_m(y,y_0,s)\sin(k_{x,m}x_0)\sin(k_{x,m}x), \tag{84}$$

where $k_{x,m} = \frac{\pi}{2w}m$, and

$$W_m(y,y_0,s) = W_m^{cc}(s)\cosh(k_{x,m}y_0)\cosh(k_{x,m}y) + W_m^{ss}(s)\sinh(k_{x,m}y_0)\sinh(k_{x,m}y). \tag{85}$$

The earlier analytical calculations were for flat geometry, which means for a vertical dechirper parallel plates that extend to infinity in both horizontal directions, and have corrugations in y vs z. ECHO2D, however, assumes smooth side walls and the wakes come as a sum of discrete modes. If the aspect ratio $2a/w$ is small enough, and a sufficient number of modes are summed, then the flat, short-range wake result and the ECHO2D result should agree. For our ECHO2D calculations, we take $a = 2$ mm and $w = 12$ mm, and the aspect ratio $2a/w$ is sufficiently small. The highest mode number in the calculations is $m = 120$; such a large number was needed for good convergence of the off-axis cases discussed below. For the ECHO2D runs, we simulated a Gaussian driving bunch with rms length of $\sigma_z = 10$ μm passing through $L = 1$ m and $L = 2$ m of structure, respectively. Then the wakefields were obtained by subtracting the 1-m results from the 2-m results. Since the catch-up distance $a^2/(2\sigma_z)$ is short compared to the structure length, this subtraction removes the transient wake contribution.

IV. EXAMPLES

A. Geometry convergence

The numerical methods used in this paper are not able to simulate open structures like those shown in Figs. 1(a)–1(c). The time-domain method can model only two horizontal corrugated plates [see Fig. 1(c)] placed between two vertical perfectly conducting walls. The frequency-domain code described above uses the rectangle geometry shown in Fig. 1(d). To calculate the wakes for nonclosed geometries like the single plate, parallel plate, and L-shape structures, we use a large dimension of the rectangle and place the charge close to the interested plates while away from others to represent the nonclosed geometries. Therefore, it is important to show that the choice of the rectangle dimension is sufficient so that those far-away plates can be neglected. To show this, we take the advantage of the zeroth-order analytical results and plot the longitudinal wake and slope of the transverse monopole wake as a function of the distance to the plate. In our calculation, we take a rectangle with half-width $b = 6$ mm and half-height $a = 2$ mm. The corrugation parameters used in this paper are listed in Table I.

TABLE I. Corrugation parameters used in the calculations.

Parameter	Value	Units
Period, p	0.5	mm
Longitudinal gap, t	0.25	mm
Depth, h	0.5	mm
Nominal distance to plate, d	0.5	mm

We first offset the beam in the vertical direction from the rectangle center to the upper plate located at $y = 2$ mm. The longitudinal wake and the slope of the vertical monopole wake as a function of the distance to the plate are shown in Fig. 2. Comparing the wakes of single plate (SP, blue circle) with L-shape (yellow line), and the wakes of parallel plate (PP, red circle) with rectangle (purple line), it can be seen that the half-width of 6 mm is sufficient and the side plates can be ignored. The wakes from the lower plate become small as the beam is far enough from the lower plate. When the distance of the beam toward the upper plate is 0.5 mm (offset = 1.5 mm), the wakes of the rectangle geometry deviate from the single-plate geometry by 5% for the longitudinal wake and 0.2% for the slope of the vertical monopole wake.

Setting the distance to the upper plate to 0.5 mm, we further shift the beam in the horizontal direction and compare the longitudinal wake and the slope of the horizontal monopole wake from the L-shape and the

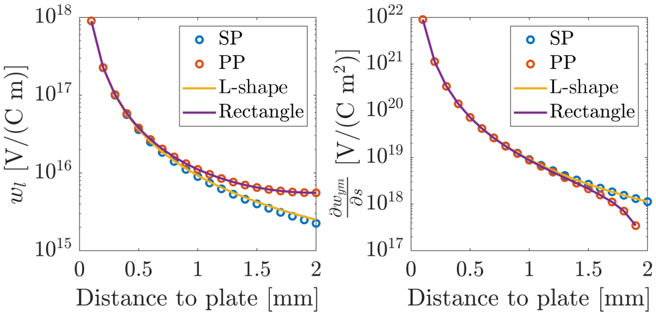

FIG. 2. Longitudinal wake (left) and the slope of vertical monopole wake (right) as a function of beam distance to the corrugated plate calculated using zeroth-order analytical formulas for single-plate (SP, blue circle), parallel-plate (PP, red circle), L-shaped (yellow line), and rectangular (purple line) structures. In the horizontal direction, the beam is at the center.

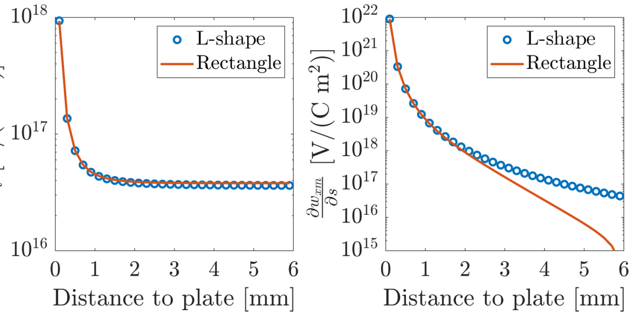

FIG. 3. Longitudinal wake (left) and the slope of transverse horizontal monopole wake (right) as a function of distance to the plate in the horizontal direction using zeroth-order analytical formulas for L-shaped (blue circle) and rectangular (red line) structures. The distance to the plate in the vertical direction is fixed at 0.5 mm.

rectangle. The results are shown in Fig. 3. Both the longitudinal wake (left) and the slope of the horizontal monopole wake (right) of the rectangular geometry converge to the L-shape geometry as the beam gets close to the right-side plate. At a distance of 0.5 mm to the plate, the deviations of wakes are below 0.2% for both the longitudinal wake and the slope of the horizontal monopole wake.

B. Single-plate structure

Using the rectangular geometry with half-width $b = 6$ mm and half-height $a = 2$ mm, we have calculated the bunch wakes of the single-plate corrugated structure for a Gaussian electron bunch with rms length $\sigma_z = 10$ μm. The bunch is placed at a distance from the upper plate of 0.5 mm. In Fig. 4, we show the longitudinal wake and transverse monopole, dipole, and quadrupole wakes obtained through analytical and numerical methods. For the analytical models, the bunch wake is obtained by convolving the charge density λ with the wake function w as

$$W(s) = \int_0^\infty w(s')\lambda(s - s')ds'. \tag{86}$$

For the numerical methods, we have used both the integral equation method and ECHO2D calculations with the same dimension. We note that for the integral equation method, all four walls have corrugations, while for the ECHO2D simulation, the two side walls are assumed smooth. As shown in the above section, the choice of the rectangle dimension ensures that the effect from the side walls is small.

It is clear from Fig. 4 that the zeroth-order analytical formulas (blue line) overestimate the longitudinal and transverse wakefields significantly. The deviations arise from the assumption of a constant longitudinal wake and constant slopes of the transverse wakes in the zeroth-order formulas. The first-order approximation (red line) improves the estimation of wakefields significantly compared with the zeroth-order approximation. The first-order results coincide with the integral equation method (yellow line) for transverse wakes, while it is slightly smaller than the integral equation method for the longitudinal wake and

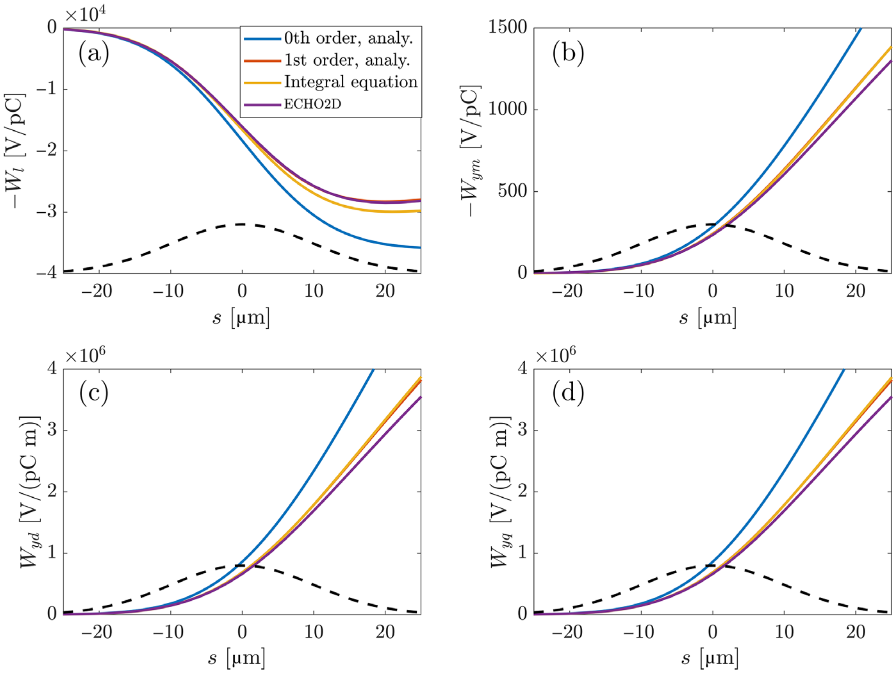

FIG. 4. Longitudinal (a) and transverse bunch wakes (b), (c), and (d) for a single-plate corrugated structure. The wakes are calculated for a Gaussian bunch (black dashes) with rms bunch length of 10 μm and the distance from the beam to the corrugated plate is 0.5 mm.

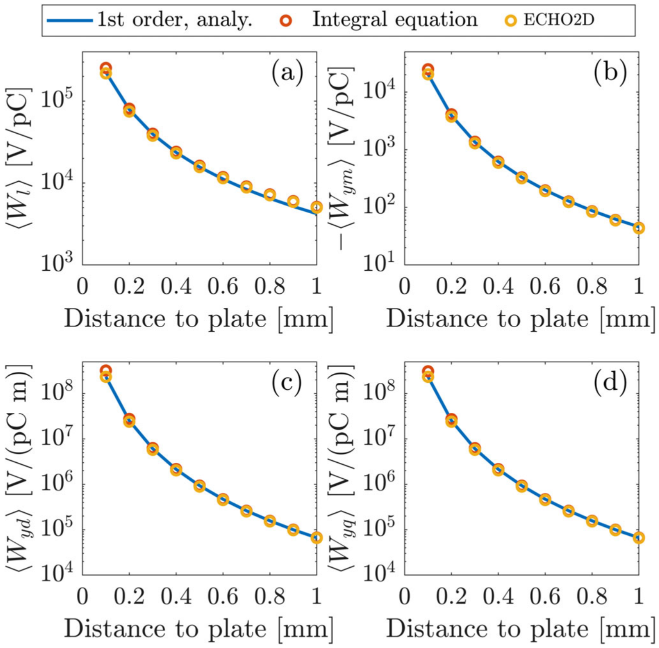

FIG. 5. Longitudinal loss factor (a) and transverse kick factors (b), (c), and (d) as a function of beam distance to the plate for a single-plate corrugated structure. Note the deviations at large distance values for the longitudinal loss factor are due to the use of rectangle geometry in numerical methods.

coincides with the ECHO2D result (purple line). This is because at the distance of 0.5 mm, the longitudinal wake still has some effect from the lower corrugated plate, as is discussed in Fig. 2. Using the first-order formula for the parallel plate (not shown in the plot) instead of the single plate, the analytical results agree with the integral equation results for all four wakes. The difference between the integral equation method and the ECHO2D simulation at the bunch tail ($3\sigma_z$ from the beam center) is about 5%.

To show the agreement of the analytical formula with numerical results at various beam positions, we performed a scan of the distance between the beam and the plate as in Fig. 2 and calculated the longitudinal loss factors (a), transverse monopole (b), dipole (c), and quadrupole (d) kick factors, with the results shown in Fig. 5. These factors were calculated from the wake potential $W(s)$ as follows:

$$\langle W(s) \rangle = \int_{-\infty}^{\infty} W(s)\lambda(s)ds. \tag{87}$$

In Fig. 5, it can be seen that good agreements between the first-order analytical formulas for a single plate (blue line), the integral equation method (red circle), and the ECHO2D simulations (yellow circle) are reached around the nominal 0.5 mm distance to the plate. At larger distance values, the deviations in the longitudinal loss factors are due to the use of rectangle geometry in numerical calculations while the analytical formula used is for single-plate structure. Again, the integral equation method and the ECHO2D results agreed well, confirming that the effect of different side walls used in these two codes can be ignored. It should be noted that when the beam is very close to the plate, at a distance of 0.1 mm in Fig. 5, the integral equation method results are about 20% larger than the ECHO2D results. The deviation could be due to the inaccuracy of the surface impedance model at a distance much smaller than the dimension of one corrugation period. The first-order analytical results agree better with the ECHO2D results at this close distance. This deviation at a small distance to the plate was also discussed in Ref. [12]. Nevertheless, the 0.1-mm distance to the plate is much smaller than the typically used 0.5 mm at several XFEL facilities where the disagreement is only on the level of a few percent.

C. L-shaped structure

For the L-shaped structure, the ECHO2D code is no longer applicable. As shown in the previous section, the agreement between the integral equation method and ECHO2D is reasonable, we will use the integral equation method alone to obtain the wakes for the L-shaped structure. We use the numerical results to validate the analytical formulas proposed earlier.

In Fig. 6, we show the longitudinal, transverse monopole, and dipole point charge wakes for the L-shaped

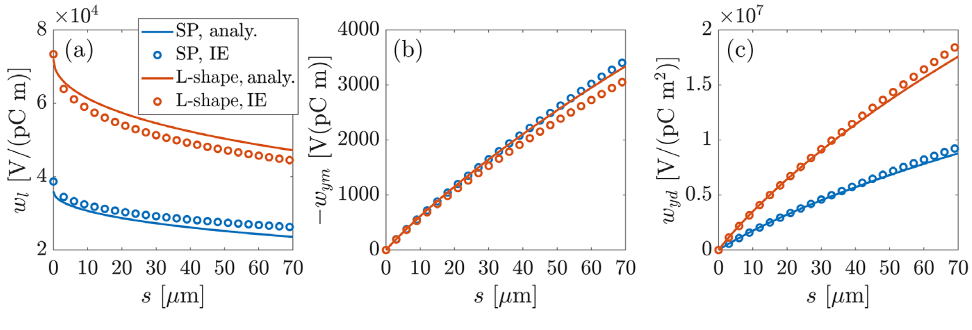

FIG. 6. Longitudinal (a) and transverse point charge wakes (b) and (c) for an L-shaped corrugated structure. The distances to both corrugated plates are 0.5 mm. For comparison, the corresponding wakes for a single-plate structure with the same distance to the plate are also plotted. Here, SP stands for single-plate and IE stands for integral equation.

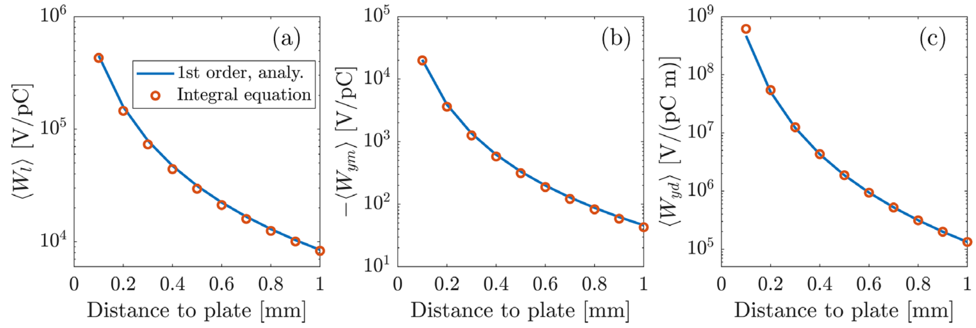

FIG. 7. Longitudinal loss factor (a) and transverse kick factors (b), and (c) as a function of beam distance to both plates in an L-shaped corrugated structure. The beam is shifted in both the x and y planes such that the distances from the beam to the two plates are kept equal.

structure with distance to both the horizontal and vertical plates being 0.5 mm. For each wake, we compare the results from the proposed analytical formula (red line) for the L-shaped structure with the integral equation method (red circle). Furthermore, it is interesting to compare the wakefields of an L-shaped structure with a single-plate structure with the same distance to its plate, shown as blue line and blue circle for the first-order analytical and integral equation results, respectively. Overall, the analytical formulas for the L-shaped structure agree well with the integral equation method. The longitudinal wake for the L-shaped structure is slightly smaller than twice of the corresponding single-plate wakes. The transverse monopole wake is slightly smaller than the monopole wake of a single-plate structure. Note that for the L-shape, the monopole wake in x also exists and has the same amplitude as y when the distances to both plates are equal. The transverse dipole wake is twice the dipole wake of the single plate. For the quadrupole wake of the L-shaped structure, the analytical formula gives exactly canceled wake, which also holds for the integral equation method.

Similar to the single-plate case, we performed a scan of the beam position in both x and y for the L-shaped structure, keeping the distance of the beam to the two plates equal. The longitudinal loss factors (a), transverse monopole (b), and dipole (c) kick factors are calculated correspondingly and shown in Fig. 7. The agreement between the analytical formulas and simulations using the integral equation methods is overall good, where the first-order analytical formula overestimates the longitudinal loss factors and transverse monopole kick factors by a few percent. At 0.1 mm distance to the plate, the deviation between the integral equation method and the analytical approximation becomes large. This is similar to what is observed in the single-plate case.

Furthermore, we also performed a scan of the beam position only in the x direction, while keeping the distance to the plate in y a constant at 0.5 mm. The longitudinal loss factors (a), transverse monopole (b), dipole (c), and quadrupole (d) kick factors are shown in Fig. 8. It can be seen that the agreement between the analytical formula and integral equation method is good except when the beam is 0.1 mm from the plate. It should also be noted that the first-order analytical formula predicts constant vertical monopole when varying the distance to the horizontal plate, while the integral equation method shows some deviation from the constant value.

From Fig. 8(d), the cancelation of the quadrupole component can be seen when the distances to both plates are equal. It is important to know how accurate the equal distance condition should reach. We define the quadrupole reduction factor as

$$F(\Delta, \bar{y}) = \max\left\{\frac{\langle W_q^{L1}(\bar{x} \pm \Delta, \bar{y}, s)\rangle}{\langle W_q^{S1}(\bar{y}, s)\rangle}\right\} \tag{88}$$

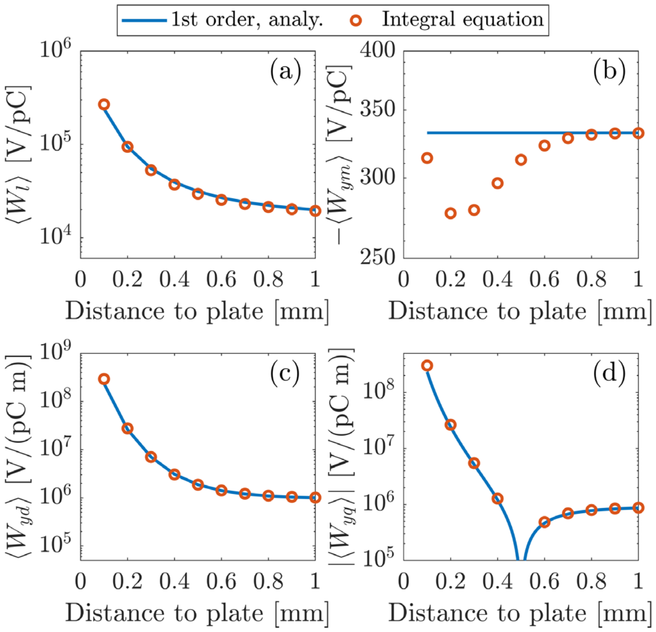

FIG. 8. Longitudinal loss factor (a) and transverse kick factors (b), (c), and (d) as a function of beam distance to the horizontal plate in an L-shaped corrugated structure. The beam is shifted in x direction only while keeping the distance to the vertical plate fixed at 0.5 mm.

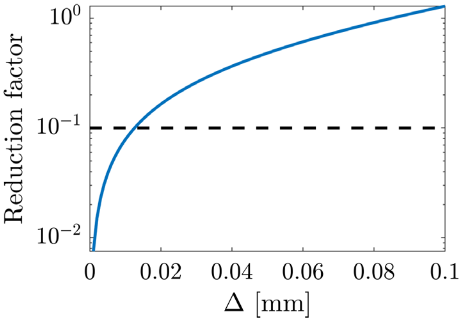

FIG. 9. Reduction factor as a function of deviation from the position where the quadrupole component can be exactly canceled.

where Δ is a small offset from the quadrupole cancelation location. Using the first-order approximation for the single-plate and L-shaped structure, we show the reduction factor as a function of the offset Δ from the 0.5-mm position in Fig. 9. At $F = 0.1$, the quadrupole component is reduced by 1 order of magnitude. The corresponding offset Δ is found to be 13 μm, which is tight but reachable in a high-energy superconducting accelerator. A slightly relaxed Δ to 20 μm allows an 85% reduction of the quadrupole component.

V. CONCLUSION

In this paper, we have performed a systematic study on the wakefields of an L-shaped corrugated structure using analytical and numerical methods. We first obtained zeroth-order analytical formulas for the L-shaped structure, along with other geometries like single plate, parallel plate, and rectangle using the conformal mapping method. Taking advantage of the zeroth-order results and the existing formulation of first-order approximation for the parallel-plate and single-plate structures, we adopted similar formal expressions and gave empirical first-order analytical approximation for the L-shaped corrugated structure. Independently, we developed a numerical integral equation method for calculating steady-state wakefields in arbitrary transverse geometry, given that the surface, like the resistive wall, corrugations, and so on, can be modeled by a given expression of surface impedance.

The results obtained are demonstrated in two numerical examples. First, we calculated the wakefields for a single-plate corrugated structure using the existing analytical formulation, the numerical method developed here, and the time-domain simulation code ECHO2D. We have shown the agreement of our numerical integral equation method with the analytical approximations and ECHO2D simulations. Then, the wakefields of the L-shaped corrugated structure were studied using the integral equation method and they confirmed the validity of the empirical first-order analytical approximation proposed in this paper. Although there is some overestimation in the longitudinal and transverse monopole wake, the first-order model is rather simple and directly follows the pattern found in the zeroth order.

Several unique features that are found in the L-shaped corrugated structure can be summarized as follows: First, the direction of the passive streaking can be varied by changing the position of the beam with respect to the horizontal and vertical corrugated plates. The total streaking strength depends on the beam distance to both plates and can be modeled by the analytical formula we gave. Second, when the beam has an equal distance to both plates compared with the single-plate structure with the same distance to the plate, the transverse quadrupole wake is canceled. The longitudinal wake is enhanced but smaller than twice the longitudinal wake from a single-plate structure; the transverse dipole wake is doubled.

The unique features of the L-shaped structure as a passive streaking device highlight a few promising applications in FELs. First, the variable polarization of the streaking could facilitate multidimensional beam phase space reconstruction. Such a streaking device is self-synchronized with the electron beam and is cost-effective. Second, the quadrupole-free streaking could ease the operation of current fresh-slice applications using single-plate configurations, which suffer from the time-dependent mismatch caused by the quadrupole wakefield. Since it removes the beam size variation along the bunch, it can also improve the resolution of the phase space diagnostic using passive streaking.

ACKNOWLEDGMENTS

We would like to thank Karl Bane, Philipp Dijkstal, Marc Guetg, Tianyun Long, and Sergey Tomin for very helpful discussions. We thank Stuart Walker for reading the manuscript and for his suggestions to improve the English of the manuscript.

APPENDIX A: APPROXIMATE BOUNDARY CONDITIONS

The surface impedance boundary condition between the tangential components of the electric field $\vec{E}$ and the magnetic field $\vec{H}$ reads

$$\vec{n} \times \vec{E} = Z_s \vec{n} \times \vec{n} \times \vec{H}, \tag{A1}$$

where $\vec{n}$ is the vector normal to the pipe surface ∂S. It reduces to the relations

$$E_z = -Z_s H_t, \qquad E_t = Z_s H_z, \tag{A2}$$

where E_t and H_t are the components of the electric and magnetic fields, respectively, tangential to the pipe surface ∂S. In order to exclude the magnetic field from the first equation, let us consider the Maxwell equations in the component form for a relativistic bunch with current density $J_z = j_z e^{i(\omega t - kz)}$, $\omega = kc$,

$$\begin{aligned}
\partial_y E_z + ikE_y &= -ikZ_0 H_x,\\
\partial_y H_z + ikH_y &= ikZ_0^{-1} E_x,\\
\partial_x E_z + ikE_x &= ikZ_0 H_y,\\
\partial_x H_z + ikH_x &= -ikZ_0^{-1} E_y,\\
\partial_x E_y - \partial_y Ex &= -ikZ_0 H_z,\\
\partial_x H_y - \partial_y H_x &= -ikZ_0^{-1} E_z + j_z.
\end{aligned} \tag{A3}$$

where Z_0 is the free-space impedance. The tangential component of the magnetic field $\vec{H}_\perp$ can be written as

$$\begin{aligned}
H_t = n_x H_y - n_y H_x &= n_x \left(\frac{1}{Z_0} E_x + \frac{1}{ikZ_0} \partial_x E_z \right)\\
&\quad + n_y \left(\frac{1}{Z_0} E_y + \frac{1}{ikZ_0} \partial_y E_z \right)\\
&= \frac{1}{Z_0} E_n + \frac{1}{ikZ_0} (n_x \partial_x E_z + n_y \partial_y E_z)\\
&= \frac{1}{Z_0} E_n + \frac{1}{ikZ_0} \partial_{\vec{n}} E_z.
\end{aligned} \tag{A4}$$

Hence the impedance boundary condition can be rewritten as

$$E_z = \frac{Z_s}{Z_0} \left(E_n + \frac{1}{ik} \partial_{\vec{n}} E_z \right), \qquad E_t = \frac{Z_s}{ik} \vec{\nabla}_\perp \vec{H}_\perp, \tag{A5}$$

where we have used Eq. (73). In the high-frequency approximation, $k \gg 1$, these equations can be simplified to the form

$$E_z = \frac{Z_s}{Z_0} E_n, \qquad E_t = 0. \tag{A6}$$

APPENDIX B: APPROXIMATION OF THE INTEGRAL OPERATORS

In order to find in Eq. (80) the unknown densities q_x and q_y, we approximate contour ∂S by N linear segments of length Δ_i, $i = 1, 2, \ldots, N$ and suggest that the densities are constant on each such segment. On the boundary ∂S, we assign N equally spaced collocation points $\vec{r}_i$, $i = 1, 2, \ldots, N$, at the centers of the segments. The singular integrals are approximated as follows:

$$\begin{aligned}
[Af](\vec{r}_i) = \int_{\partial S} \log|\vec{r}_i - \vec{r}'| f(\vec{r}') ds(\vec{r}') &= \left(\log \frac{\Delta_i}{2} - 1 \right) \Delta_i\\
&\quad + \sum_{j=1, j\neq i}^{N} \log|\vec{r}_i - \vec{r}_j| f(\vec{r}_j) \Delta_j,
\end{aligned} \tag{B1}$$

$$\begin{aligned}
\partial_x [Af](\vec{r}_i) = [\partial_x Af](\vec{r}_i) + \pi n_x(\vec{r}_i) f(\vec{r}_i) &= \pi n_x(\vec{r}_i) f(\vec{r}_i)\\
&\quad + \sum_{j=1, j\neq i}^{N} \frac{x_i - x_j}{|\vec{r}_i - \vec{r}_j|^2} f(\vec{r}_j) \Delta_j,
\end{aligned} \tag{B2}$$

$$\begin{aligned}
\partial_y [Af](\vec{r}_i) = [\partial_y Af](\vec{r}_i) + \pi n_y(\vec{r}_i) f(\vec{r}_i) &= \pi n_y(\vec{r}_i) f(\vec{r}_i)\\
&\quad + \sum_{j=1, j\neq i}^{N} \frac{y_i - y_j}{|\vec{r}_i - \vec{r}_j|^2} f(\vec{r}_j) \Delta_j,
\end{aligned} \tag{B3}$$

where $n_x(\vec{r}_i)$, $n_y(\vec{r}_i)$ are components of normal $\vec{n}$ to the boundary at the point $\vec{r}_i$. The obtained matrix equation is solved by the direct method of LU factorization with partial pivoting.

[1] K. Bane and G. Stupakov, Corrugated pipe as a beam dechirper, Nucl. Instrum. Methods Phys. Res., Sect. A **690**, 106 (2012).

[2] P. Emma, M. Venturini, K. L. F. Bane, G. Stupakov, H.-S. Kang, M. S. Chae, J. Hong, C.-K. Min, H. Yang, T. Ha, W. W. Lee, C. D. Park, S. J. Park, and I. S. Ko, Experimental Demonstration of Energy-Chirp Control in Relativistic Electron Bunches Using a Corrugated Pipe, Phys. Rev. Lett. **112**, 034801 (2014).

[3] H. Deng, M. Zhang, C. Feng, T. Zhang, X. Wang, T. Lan, L. Feng, W. Zhang, X. Liu, H. Yao, L. Shen, B. Li, J. Zhang, X. Li, W. Fang, D. Wang, M.-e. Couprie, G. Lin, B. Liu, Q. Gu, D. Wang, and Z. Zhao, Experimental Demonstration of Longitudinal Beam Phase-Space Linearizer in a Free-Electron Laser Facility by Corrugated Structures, Phys. Rev. Lett. **113**, 254802 (2014).

[4] A. A. Lutman, T. J. Maxwell, J. P. MacArthur, M. W. Guetg, N. Berrah, R. N. Coffee, Y. Ding, Z. Huang, A. Marinelli, S. Moeller, and J. C. U. Zemella, Fresh-slice multicolour x-ray free-electron lasers, Nat. Photonics **10**, 745 (2016).

[5] S. Bettoni, P. Craievich, A. Dax, R. Ganter, M. W. Guetg, M. Huppert, F. Marcellini, R. Neto Pestana, S. Reiche, E. Prat, A. Trisorio, C. Vicario, and A. A. Lutman, Experimental demonstration of two-color x-ray free-electron-laser pulses via wakefield excitation, Phys. Rev. Accel. Beams **24**, 082801 (2021).

[6] A. A. Lutman, M. W. Guetg, T. J. Maxwell, J. P. MacArthur, Y. Ding, C. Emma, J. Krzywinski, A. Marinelli, and Z. Huang, High-Power Femtosecond Soft X Rays from Fresh-Slice Multistage Free-Electron Lasers, Phys. Rev. Lett. **120**, 264801 (2018).

[7] Y.-C. Chao, W. Qin, Y. Ding, A. A. Lutman, and T. Maxwell, Control of the Lasing Slice by Transverse Mismatch in an X-Ray Free-Electron Laser, Phys. Rev. Lett. **121**, 064802 (2018).

[8] J. Seok, M. Chung, H.-S. Kang, C.-K. Min, and D. Na, Use of a corrugated beam pipe as a passive deflector for bunch length measurements, Phys. Rev. Accel. Beams **21**, 022801 (2018).

[9] P. Dijkstal, A. Malyzhenkov, P. Craievich, E. Ferrari, R. Ganter, S. Reiche, T. Schietinger, P. Juranić, and E. Prat, Self-synchronized and cost-effective time-resolved measurements at x-ray free-electron lasers with femtosecond resolution, Phys. Rev. Res. **4**, 013017 (2022).

[10] S. Bettoni, P. Craievich, A. A. Lutman, and M. Pedrozzi, Temporal profile measurements of relativistic electron bunch based on wakefield generation, Phys. Rev. Accel. Beams **19**, 021304 (2016).

[11] Z. Zhang, K. Bane, Y. Ding, Z. Huang, R. Iverson, T. Maxwell, G. Stupakov, and L. Wang, Electron beam energy chirp control with a rectangular corrugated structure at the linac coherent light source, Phys. Rev. ST Accel. Beams **18**, 010702 (2015).

[12] K. Bane, G. Stupakov, and I. Zagorodnov, Analytical formulas for short bunch wakes in a flat dechirper, Phys. Rev. Accel. Beams **19**, 084401 (2016).

[13] K. Bane, G. Stupakov, and I. Zagorodnov, Wakefields of a beam near a single plate in a flat dechirper, SLAC National Accelerator Laboratory Technical Report No. SLAC-PUB-16881, 2016.

[14] Z. Guo, M. W. Guetg, Y. Ding, A. Marinelli, J. Wu, Z. Huang, and A. A. Lutman, Simulation analysis and optimization of fresh-slice multistage free-electron lasers, Phys. Rev. Accel. Beams **23**, 031304 (2020).

[15] W. Qin, Y. Ding, A. A. Lutman, and Y.-C. Chao, Matching-based fresh-slice method for generating two-color x-ray free-electron lasers, Phys. Rev. Accel. Beams **20**, 090701 (2017).

[16] W. Qin, M. Guetg, W. Decking, E. Gjonaj, N. Golubeva, J. Guo, S. Liu, T. Wohlenberg, and I. Zagorodnov, Corrugated structure system for fresh-slice applications at the European XFEL, in *Proceedings of FEL'22, Trieste, Italy* (JACoW, Geneva, Switzerland, 2022), paper MOP38.

[17] C.-K. Ng and K. Bane, Wakefield Computations for a corrugated pipe as a beam dechirper for FEL applications, in *Proceedings of the 25th Particle Accelerator Conference, PAC-2013, Pasadena, CA, 2013* (IEEE, New York, 2013), p. 877.

[18] A. Novokhatski, Wakefield potentials of corrugated structures, Phys. Rev. ST Accel. Beams **18**, 104402 (2015).

[19] I. Zagorodnov, K. L. F. Bane, and G. Stupakov, Calculation of wakefields in 2D rectangular structures, Phys. Rev. ST Accel. Beams **18**, 104401 (2015).

[20] K. Bane and G. Stupakov, Dechirper wakefields for short bunches, Nucl. Instrum. Methods Phys. Res., Sect. A **820**, 156 (2016).

[21] K. Bane and G. Stupakov, Using surface impedance for calculating wakefields in flat geometry, Phys. Rev. ST Accel. Beams **18**, 034401 (2015).

[22] S. S. Baturin and A. D. Kanareykin, Cherenkov Radiation from Short Relativistic Bunches: General Approach, Phys. Rev. Lett. **113**, 214801 (2014).

[23] S. S. Baturin and A. D. Kanareykin, New method of calculating the wakefields of a point charge in a waveguide of arbitrary cross section, Phys. Rev. Accel. Beams **19**, 051001 (2016).

[24] S. S. Baturin, G. Andonian, and J. B. Rosenzweig, Analytical treatment of the wakefields driven by transversely shaped beams in a planar slow-wave structure, Phys. Rev. Accel. Beams **21**, 121302 (2018).

[25] P. K. Kythe, *Handbook of Conformal Mappings and Applications* (CRC Press, New York, 2019), https://doi.org/10.1201/9781315180236.

[26] I. Zagorodnov, M. Dohlus, and T. Wohlenberg, Short-range longitudinal wake function of undulator lines at the European X-Ray Free Electron Laser, Nucl. Instrum. Methods Phys. Res., Sect. A **1043**, 167490 (2022).

[27] M. Dohlus, Impedance of beam pipes with smooth shallow corrugations, Deutsches Elektronen-Synchrotron DESY Technical Report No. 2001-26, 2001.

[28] K. Bane and G. Stupakov, Roughness tolerance studies for the undulator beam pipe chamber of LCLS-II, SLAC National Accelerator Laboratory Technical Report No. SLAC-PUB-15951, 2014.

[29] G. Stupakov, Coupling impedance of a periodic array of diaphragms, in *Proceedings of the Particle Accelerator Conference, Dallas, TX, 1995* (IEEE, New York, 1995), Vol. 5, pp. 3303–3305.

[30] G. Stupakov and K. L. F. Bane, Surface impedance formalism for a metallic beam pipe with small corrugations, Phys. Rev. ST Accel. Beams **15**, 124401 (2012).

[31] I. Zagorodnov, Analytical Impedance Models for Very Short Bunches, in *Proceedings of ICFA Mini-Workshop on Impedances and Beam Instabilities in Particle Accelerators, Benevento, Italy* (CERN, Geneva, 2018), pp. 133–140.

[32] K. Yokoya and K. Bane, The longitudinal high-frequency impedance of a periodic accelerating structure, in *Proceedings of the 1999 Particle Accelerator Conference, New York, 1999* (IEEE, Piscataway, 1999), p. 1725.

[33] D. Colton and R. Kress, Integral equation methods in scattering theory (Society for Industrial and Applied Mathematics, Philadelphia, PA, 2013), https://doi.org/10.1137/1.9781611973167.